Electronic Supplementary Information

Ultrathin Amorphous Cobalt-Vanadium Hydr(oxy)oxide Catalysts for Oxygen Evolution Reaction

Juzhe Liu,‡[a] Yongfei Ji, ‡[b] Jianwei Nai,‡[a] Xiaogang Niu,[a] Yi Luo,[b, c] Lin Guo*[a] and Shihe Yang*[d]*

a. School of Chemistry, Beijing Advanced Innovation Center for Biomedical Engineering, Beihang University, Beijing 100191, China. E-mail: guolin@buaa.edu.cn
b. Department of Theoretical Chemistry and Biology, School of Biotechnology, KTH Royal Institute of Technology, Stockholm, SE-106 91, Sweden.
c. Hefei National Laboratory for Physical Sciences at the Microscale, University of Science and Technology of China, Hefei 230026, China. E-mail: yiluo@ustc.edu.cn
d. Department of Chemistry, The Hong Kong University of Science and Technology, Clear Water Bay, Kowloon, Hong Kong. China. E-mail: chsyang@ust.hk.
‡ The authors contributed equally to this work.

1. Methods

Materials. cobalt chloride hexahydrate ($CoCl_2$•$6H_2O$), sodium hydroxide (NaOH), ammonium vanadate (NH_4VO_3) and other reagents are all analytical grade and used without further purification. Commercial $Co(OH)_2$ (99.9%)and IrO_2 (99%) were purchased from Alfa Aesar.

Synthesis of amorphous CoV-UAH. In a typical procedure, 0.5 mM $CoCl_2·6H_2O$ was added to solution of 50 ml deionized water under constant stirring. And then 1 mM NaOH and 0.17 mM NH_4VO_3 were loaded into a jar containing 20 mL of distilled water to form a transparent solution after stirring for several minutes. Subsequently, the mixture solution was dropwise added to the $CoCl_2$ solution in a water bath at 30 ºC and brown yellow precipitation was formed. After 15 min of stirring, the sample was washed by deionized water three times. In addition, cobalt-vanadium hydr(oxy)oxide with different Co:V ratios of 10:1, 10:5 and 10:7 were synthesized by regulating the dosing ratio of Co and V sources.

Synthesis of Co-UH. As a reference, for preparation of α-$Co(OH)_2$, the same process were followed except NH_4VO_3 was added. In addition, the obtained green precipitation was washed by mixed solution of ethanol and water (9:1) three times.

Synthesis of crystalline CoV-C. CoV-C was prepared by heat treatment of CoV-UAH at 600 ºC for 3 h in air.

Synthesis of crystalline V_2O_5. Crystalline vanadium pentoxide powder was prepared for comparison purposes by heat treatment of NH_4VO_3 powder at 600 ºC for 3 h in air.

Synthesis of crystalline VO_2. VO_2 was fabricated via a modified hydrothermal method.[S1] 2.0 mM NH_4VO_3 powder was added to 40 ml oxalic acid in aqueous solution with continuous stirring to form yellow slurry. Then the slurry was transferred to a 50 ml autoclave with a Teflon liner. The autocalve was sealed and maintained at 180 ºC for 24h and then cooled to room temperature naturally. The products were collected and washed with distilled water and ethanol three times, and dried at 70 ºC under vacuum for 10 h.

Synthesis of crystalline $Co_3V_2O_8$. $Co_3V_2O_8$ was fabricated followed previous report.[S2] In a typical procedure, 3 mmol of $CoCl_2·6H_2O$ was dissolved in 20 mL distilled water and stirred at 70 ºC. 20 mL distilled water containing 2 mmol of $Na_3VO_4·12H_2O$ was added dropwise and the resulting suspension was stirred at 70 ºC for 2 h. The products of the reaction were washed with distilled water three times, and the brown powders were collected after washing/centrifugation and drying at 60 ºC for 12 h. The sample was 600 ºC for 2 h in air.

Synthesis of CoOOH. The CoOOH was fabricated according to reported methods.[S3-5] In brief, bulk $Co(OH)_2$ was firstly prepared by homogeneous precipitation and then was oxidized into CoOOH using NaClO as an oxidizing agent. The average valence state of the Co species in the CoOOH was determined to be +3.26 by iodometric titration.

Synthesis of IrO_2. IrO_2 used for catalytic activity comparison was obtained by ball-milling treatment of commercial IrO_2 lasting 20 min.

Characterizations. Transmission electron microscopy (TEM) and selected area electron diffraction (SAED) were carried out on a JEOL JEM-2100 microscope. X-ray powder diffraction (XRD) patterns was obtained by a Shimadzu Xlab6000 X-ray diffractometer and the Data were collected in Bragg-Brentano mode with a scan rate of 5° s^{-1}. The morphologies and element composition of the synthesized samples were prepared on Si substrates and studied by a JEOL JSM-7500F cold-field emission scanning electron microscope (CFESEM). X-ray absorption spectroscopy (XAS) spectra were obtained from the Beijing Synchrotron Radiation Facility at 1W1B. The electron beam energy is 2.5 GeV and the current is between 160 and 250 mA. We ran Co K-edge EXAFS in the range from 7525 eV to 8507 eV and V K-edge EXAFS in the range form 5265 eV to 6265 eV in fluorescence mode and with a step-size of 0.7 eV at the near edge. The set up for the *in-situ* XAS is illustrated in Fig.S24. X-ray photon spectroscopy (XPS) was recorded by a Thermo Scientific ESCALAB 250 Xi XPS system, where the analysis chamber was $1.5×10^{-9}$ mbar and the size of X-ray spot was 500 μm. All the spectra were referenced to the C 1s at binding energy (BE) of 284.8 eV.

EXAFS Analysis. The XAS raw data were background-subtracted, normalized, and Fourier transformed by standard procedures with the ATHENA program in IFEFFIT software.[S6,7] Edge step normalization for each spectrum was performed by subtracting the pre-edge and post-edge backgrounds. k^3-weighted χ(k) data in the k-space ranging from 2.455–12.342 $Å^{-1}$ for Co and 2.791–11.511 $Å^{-1}$ for V were Fourier transformed to real (R) space using a hanning windows (dk = 1.0 $Å^{-1}$) to separate the EXAFS contributions from different coordination shells. We used ARTEMIS module of IFEFFIT to perform the least-squares curve parameter fitting to obtain the quantitative structural parameters around Co and V atoms.[S8] Effective scattering amplitudes and phase-shifts for the Co-O and V-O pairs were calculated with the ab initio code FEFF8.0.[S9,10] A nonlinear least-squares algorithm was applied for the curve fitting of EXAFS in R-space between 1.0 and 2.0 Å for the Co and V K-edge. Here, the amplitude reduction factor S_0^2 of 0.77 was obtained from the fitting result of commerical $Co(OH)_2$ and in accord with previous work.[S11-13] The atomic structure parameters of CN (coordination number), R (Å) (bond distance), Debye-Waller factor (σ^2) and edge-energy shift (ΔE) were estimated by fitting analysis employing the Artemis (version 0.8.011) module implemented in the IFEFFIT package. All EXAFS data were fitted to the Fourier transforms of χ(k) using k-weights of 1, 2, and 3 simultaneously.

DFT simulations. The calculations were carried out with density functional theory implanted in VASP[S14-17]. PBE[S18] exchange-correlation functional and PAW[S19] pseudo-potential were adopted. An energy cutoff of 460 eV was applied for the plan-wave basis set. CoOOH was described by five-layer (104) surface with a vacuum layer of 12Å. CoOOH is the most stable phase of Cobalt oxide under oxygen evolution reaction conditions, and (104) is its most stable and active facets[S20]. A 2×2 supercell was used, and the Brillouin zone is sampled by a 3×3 Monkhorst-Pack grid. One of the top layer Co atoms was substituted by V to present V doped CoOOH. To describe the transition metal elements, DFT+U[S21] method have been used with the *ab initio* U values[S22-24], U – J = 3.3 eV for Co and U – J = 3.4 eV for V species. The structures were optimized (with the bottom three layers fixed) until the maxima force on the atoms was smaller than 0.02eV/Å. The following mechanism for water oxidation was adopted[S25]. The calculation of the reaction free energy with the zero point energy and entropy corrections followed the same procedure in ref[S24]. ΔG_4 is defined as 4.92eV-ΔG_1-ΔG_2-ΔG_3 to avoid the calculation of the energy of O_2 molecule.

Electrochemical Measurements. We adopted catalysts (1 mg) were dispersed in solvent consisted of 350 μL of deionized water, 135 μL of alcohol and 15 μL of 5 wt% Nafion solution. After sonication for 10 min, 20 μL of homogeneous ink was drop-casted onto the glassy carbon electrode of 5 mm in diameter with the loading of 0.2 mg cm^{-2}. 250 μL ink was drop dried onto a Au foam with a fixed area of 0.5 cm^2 (loading 1 mg cm^{-2}). In *in-situ* XAS test, 50 μL ink was drop-casted onto the carbon paper electrode to ensure the same loading of 0.2 mg cm^{-2}. After drying at room temperature, the fabrication of working electrodes was finished. Electrolysis experiments were performed in a standard three-electrode system controlled by Pine Instruments electrochemistry workstation. Pt wire work as a counter electrode and our reference electrode is Ag/AgCl electrode. All potentials measured were calibrated to the reversible hydrogen electrode (RHE) using the following equation: $E_{RHE} = E_{Ag/AgCl} + 0.197$ V +0.059 pH, where pH = 14 in 1 M KOH solution. Working electrode rotated at 1600 rpm to get rid of the generated oxygen bubbles. Electrochemical tests were carried out in 1 M KOH electrolytes. LSVs were performed at 2 mV s^{-1} for polarization curves and 0.1 mV s^{-1} for Tafel plots after the pretreatment of performing LSVs at 20 mV s^{-1} for 10 cycles until the oxygen evolution currents showed negligible change. The electrochemical impedance spectroscopy (EIS) data were collected for the electrodes under 0.5 V vs. Ag/AgCl on glass carbon electrode. The amplitude of the sinusoidal wave was 10 mV, and the frequency scan range was from 100 kHz to 0.01 Hz. The measured impedance data were fitted using a series R(QR)(QR) equivalent circuit. All polarization curves were corrected with 95% *iR*-compensation and the R in 1 M KOH is 6 ohms.

Turnover frequency (TOF) calculation of the catalysts: The TOF values are calculated from the equation below:

$$\text{TOF} = J \times A/(4 \times F \times n) \quad \text{(Eq. S1)}$$

Where J is the current density at given overpotentials, A is the surface area of the electrode, F is the Faraday constant (a value of 96485 C mol^{-1}), and n is the number of moles of metal on the electrode, which was measured by inductively coupled plasma-mass spectrometry (ICP-MS).

The Faradaic efficiency was obtained based on the previous literatures[S26].

$$\text{Faradaic efficiency} = I_{ring}/(C_c \times I_{disk}) \quad \text{(Eq. S2)}$$

Here, the I_{ring} is the collection current on Pt ring electrode at a constant potential of 0.4 V vs. RHE. I_{disk} is the current on glassy carbon disk electrode. C_c is the oxygen collection coefficient of 0.2 for this type of electrode configuration.

2. Results and Discussion

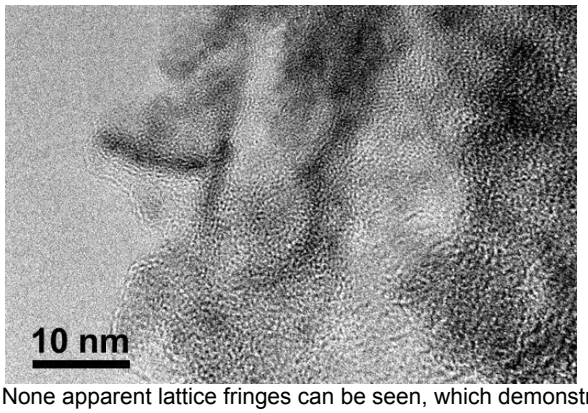

Fig. S1 HRTEM of CoV-UAH. None apparent lattice fringes can be seen, which demonstrates its amorphous structure.

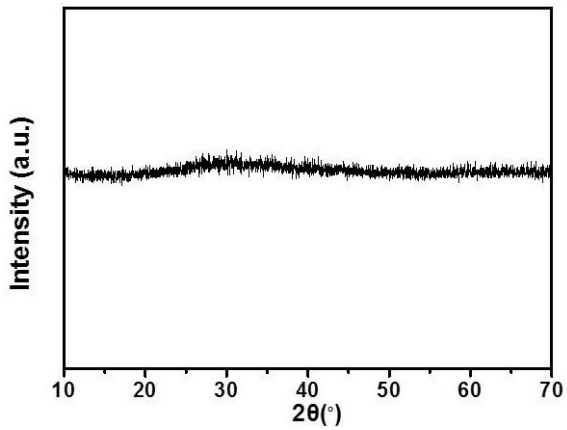

Fig. S2 XRD of CoV-UAH. None sharp Bragg reflection peak is observed, confirming its amorphous state.

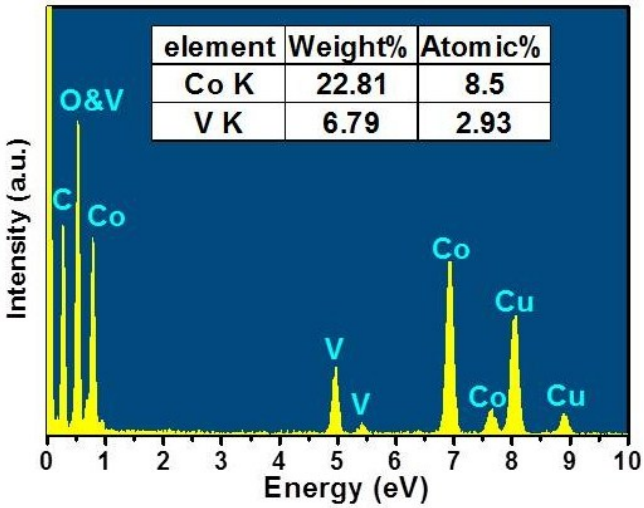

Fig. S3 EDS measurements of CoV-UAH. This reveals the composition ratio of Co and V as about 10: 3.5 which is approximate to the feed composition.

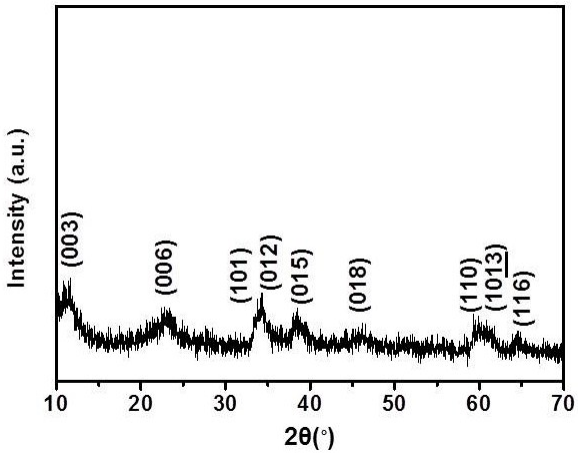

Fig. S4 XRD pattern of Co-UH. From the XRD pattern, this product can be rationally identified as α-$Co(OH)_2$ but with low crystallinity.

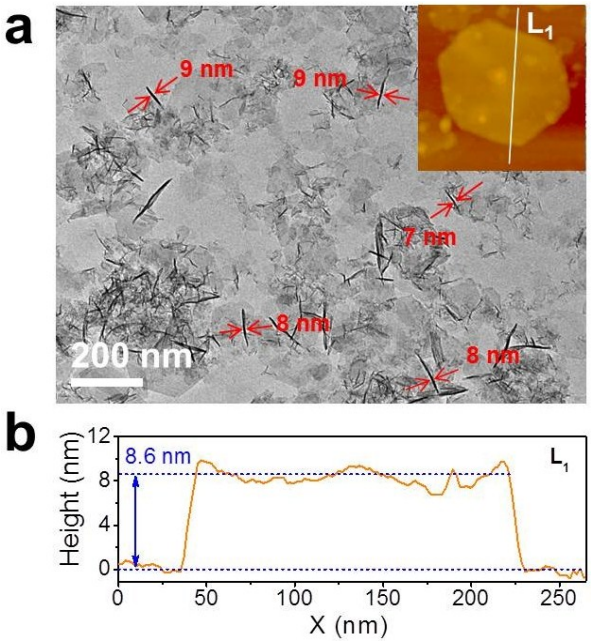

Fig. S5 Morphology and thickness characterization of Co-UH (a) TEM image of Co-UH. The arrows mark the thickness of upstanding nanosheets. And the inset is the AFM image of as-prepared Co-UH, showing measured dimension of the flake. (b) Corresponding height profile of Co-UH.

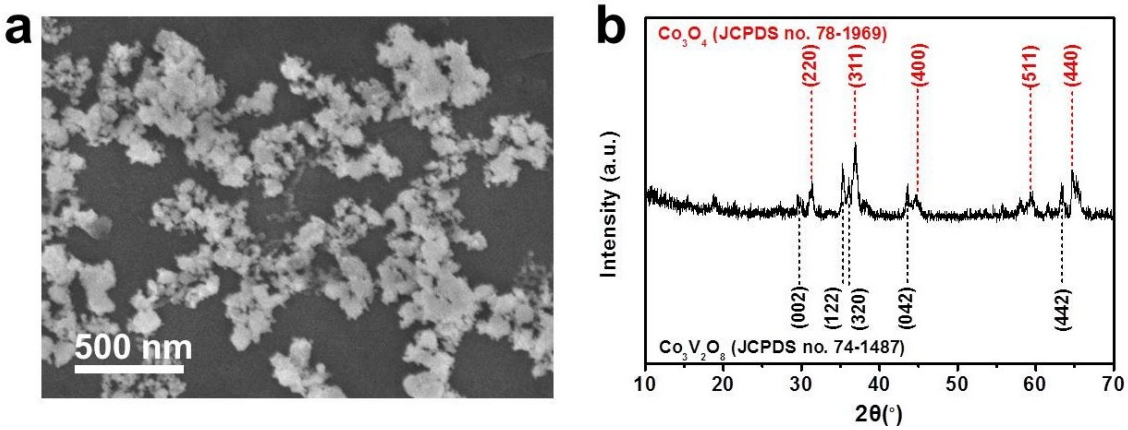

Fig. S6 Morphology and structure characterization of CoV-C. (a) SEM image of CoV-C. It can be seen that, after annealing in air at 600 °C for 3 h, CoV-UAH transformed into agglomerate powers with wide size distribution. (b) XRD pattern. The XRD pattern shows the CoV-C is consisted of Co_3O_4 and $Co_3V_2O_8$ phase.

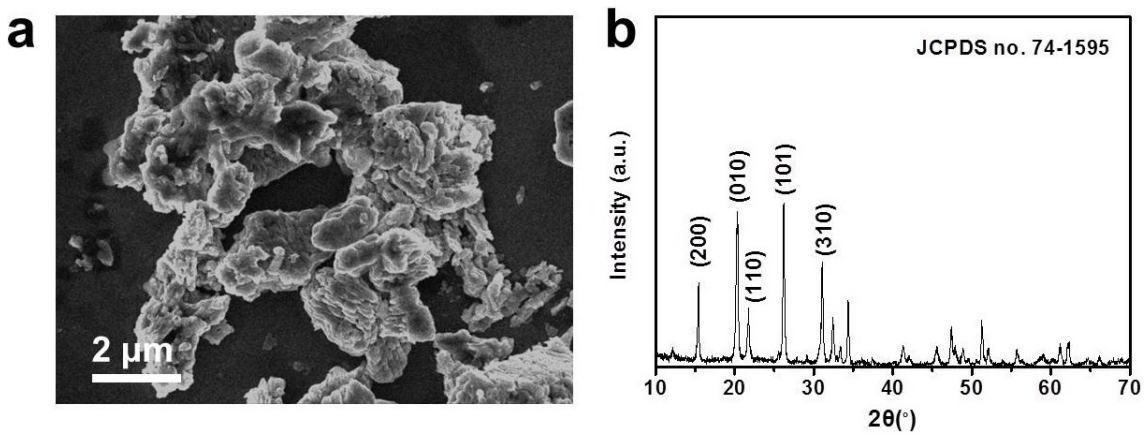

Fig. S7 Morphology and structure characterization of V_2O_5. (a) SEM image and (b) XRD pattern of V_2O_5. By using a typical method of annealing NH_4VO_3 in air, we obtained bulk V_2O_5 with high crystallinity.

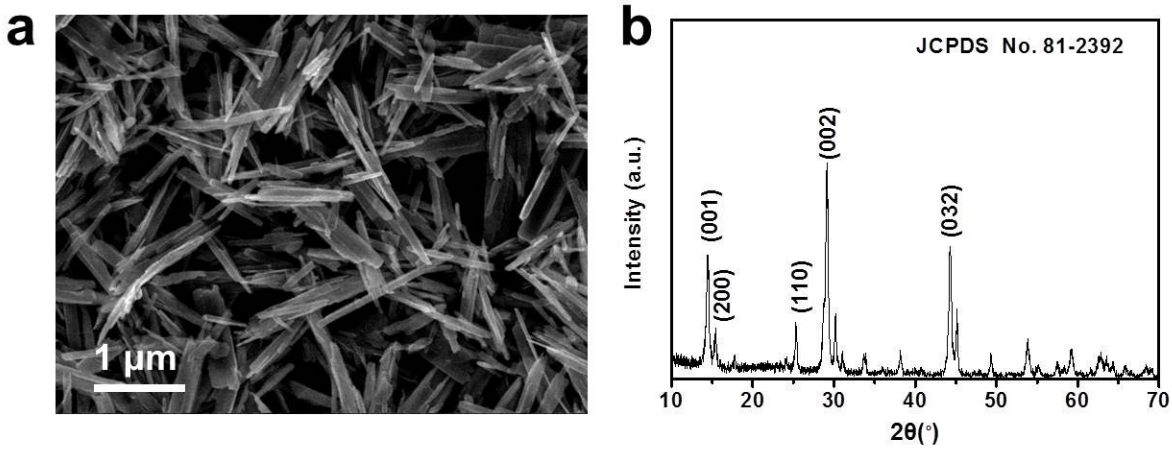

Fig. S8 Morphology and structure characterization of VO_2. (a) SEM image and (b) XRD pattern of VO_2. The prepared VO_2 is nanobelt structure with typical XRD diffraction peaks.

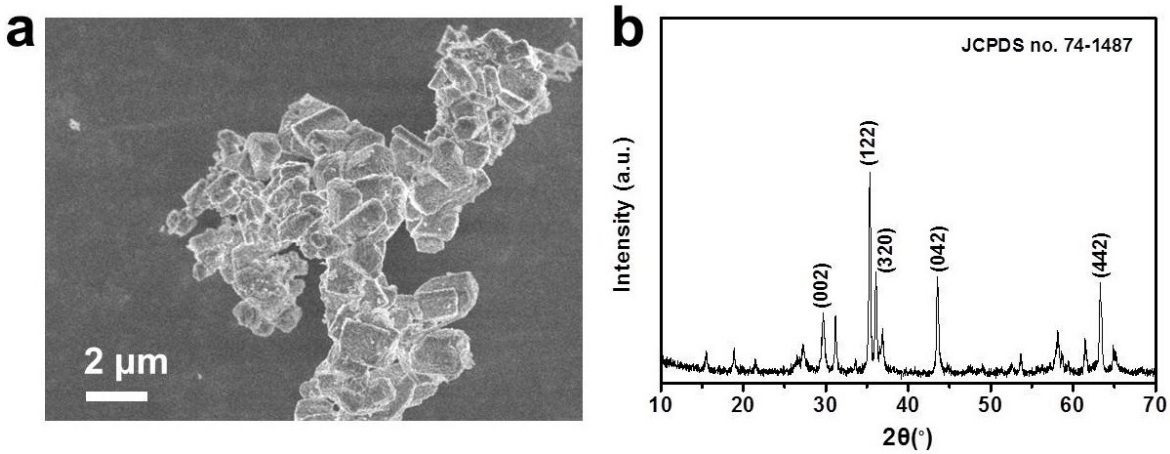

Fig. S9 Morphology and structure characterization of $Co_3V_2O_8$. (a) SEM image and (b) XRD pattern of $Co_3V_2O_8$. The prepared $Co_3V_2O_8$ is bulk structure with typical XRD diffraction peaks.

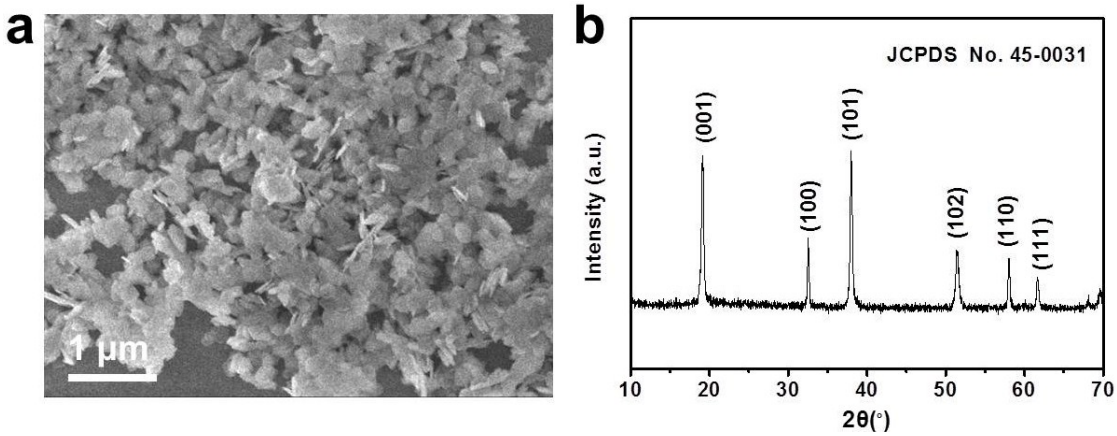

Fig. S10 Morphology and structure characterization of commercial $Co(OH)_2$. (a) SEM image and (b) XRD pattern of $Co(OH)_2$. The $Co(OH)_2$ shows hexagonal sheet-like structure and typically XRD pattern.

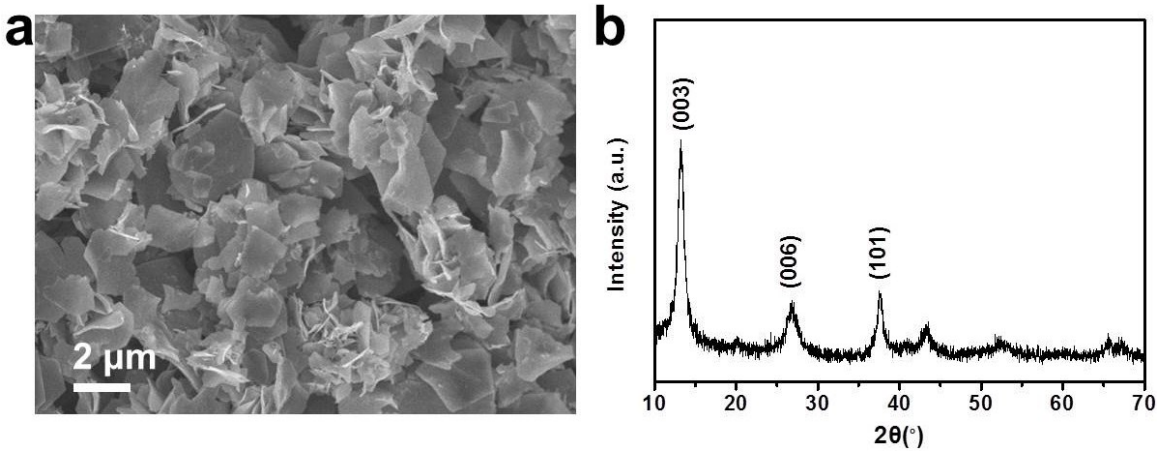

Fig. S11 Morphology and structure characterization of CoOOH. (a) SEM image and (b) XRD pattern of CoOOH. The CoOOH shows lamellar structure with the size of about 1-4 μm as shown in the SEM image and a highly (0 0 n) preferred orientation in XRD pattern.

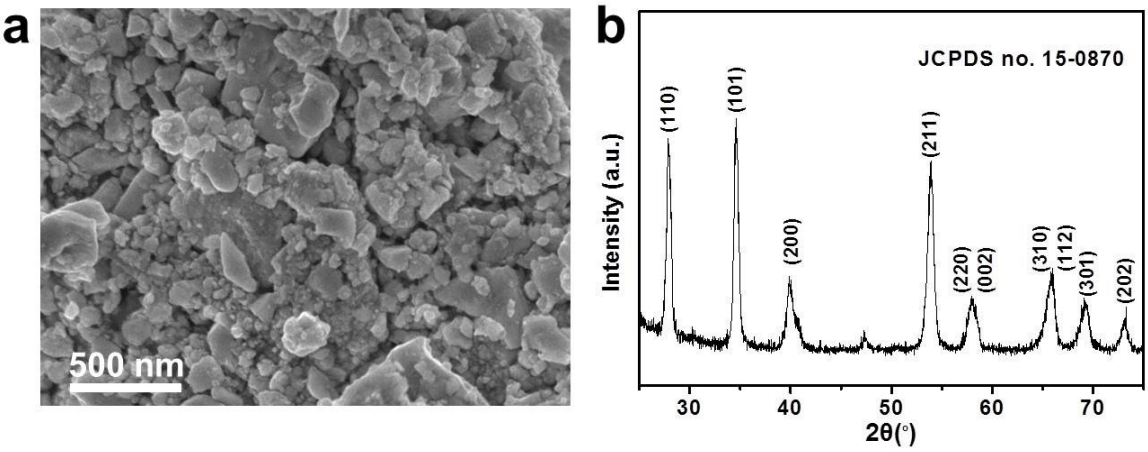

Fig. S12 The physical characterization data of IrO_2 after ball-milling treatment. (a) SEM image and (b) XRD pattern. The processed IrO_2 is composed of nanoparticles with wide size distribution from tens to hundreds nanometers and remains crystalline structure of IrO_2.

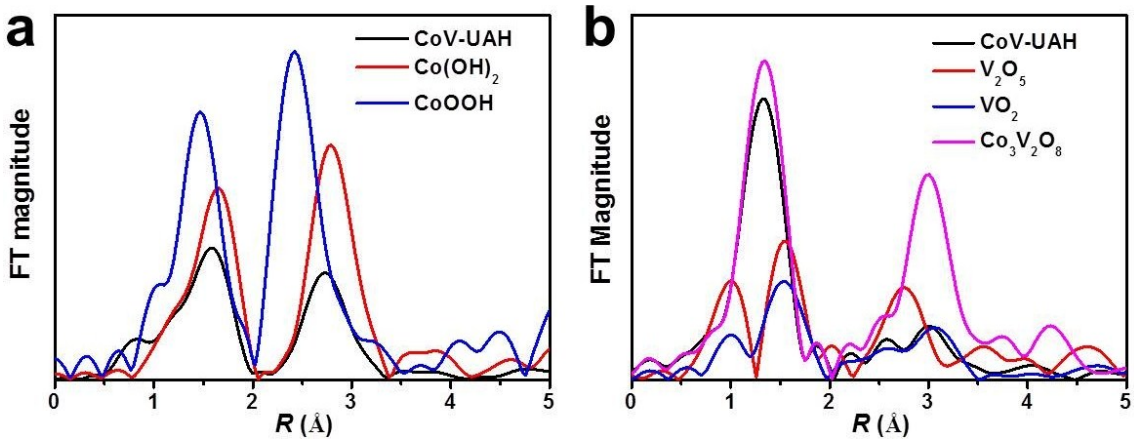

Fig. S13 EXAFS spectra of Co K-edge and V K-edge of CoV-UAH and its counterparts. (a) Comparison of Co K-edge EXAFS data in R-space collected on as-prepared CoV-UAH and the its counterparts. In comparison with $Co(OH)_2$, CoV-UAH shows lower peak amplitude and left-shift peak position. (b) Comparison of V K-edge EXAFS data in R-space collected on as-prepared CoV-UAH and the its counterparts. Only one apparent V-O peak can be observed for CoV-UAH which indicates vanadium ions are highly dispersed.

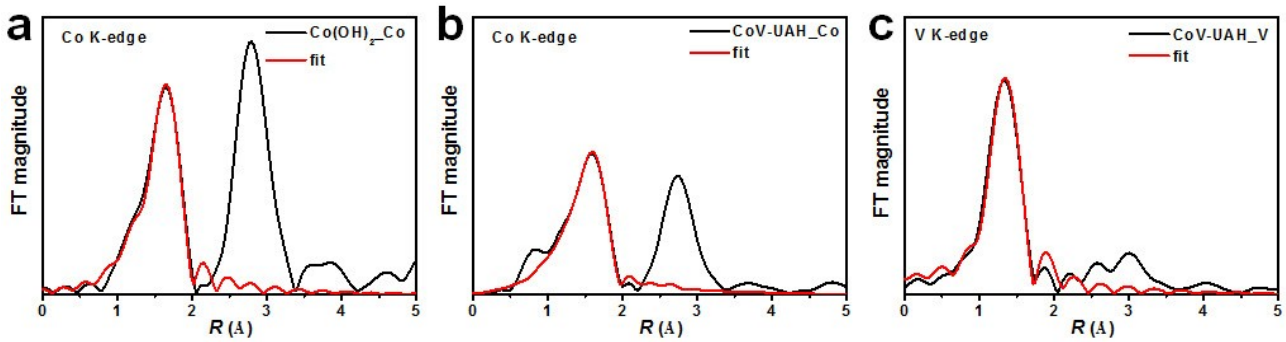

Fig. S14 The fitting results of EXAFS spectra. (a) EXAFS curves-fitting result of the Co K-edge of $Co(OH)_2$. (b) EXAFS curves-fitting result of the of Co K-edge for CoV-UAH. (c) EXAFS curves-fitting result of the V K-edge for CoV-UAH.

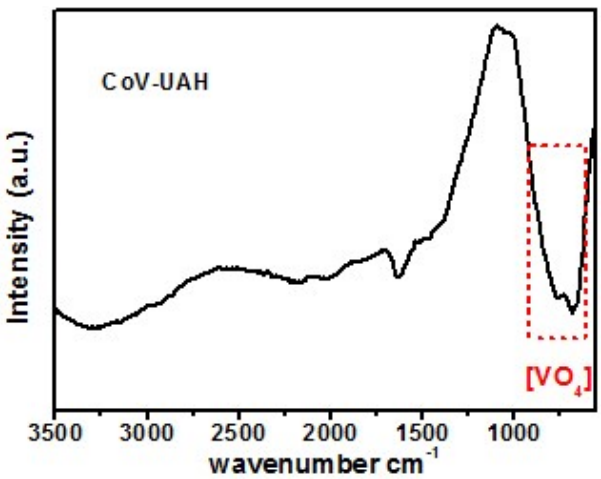

Fig. S15 Fourier transform infrared (FT-IR) spectra of CoV-UAH. According to previous reports, the vibration bands in the range of 930 - 650 cm^{-1} are attributed to tetrahedral $[VO_4]$.[S27]

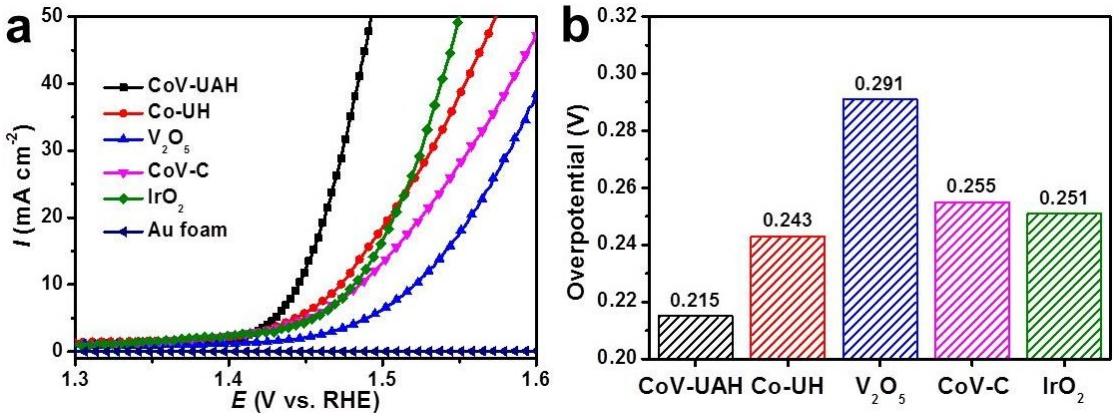

Fig. S16 Activity performance of CoV-UAH on Au plated Ni foam. (a) The OER polarization curve of catalysts loaded on Au plated Ni foam (scan rate 1 mV s^{-1}) and the bare Au plated Ni foam is also tested under the same condition. (b) Overpotentials obtained from OER ploarization curves at the current density of 10 mA cm^{-2} tested on Au plated Ni foam, without *iR*-correction.

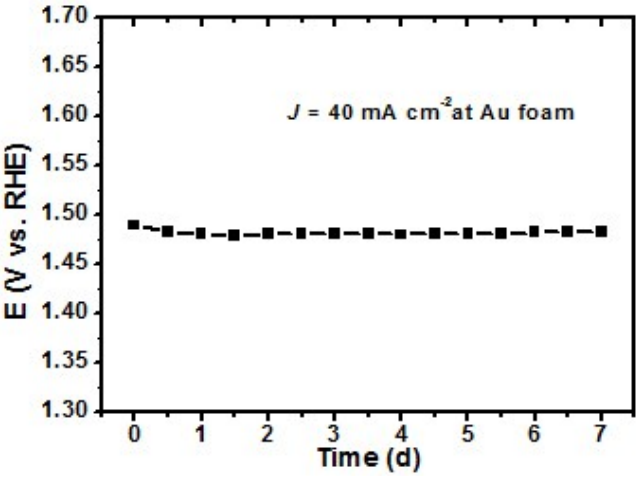

Fig. S17 Stability performance of CoV-UAH. Long-time chronopotentiometry was carried out on Au plated Ni foam at 40 mA cm^{-2} lasting about 7 days (170 h) and no appreciable increase was observed in potential in this time interval, suggesting its excellent stability.

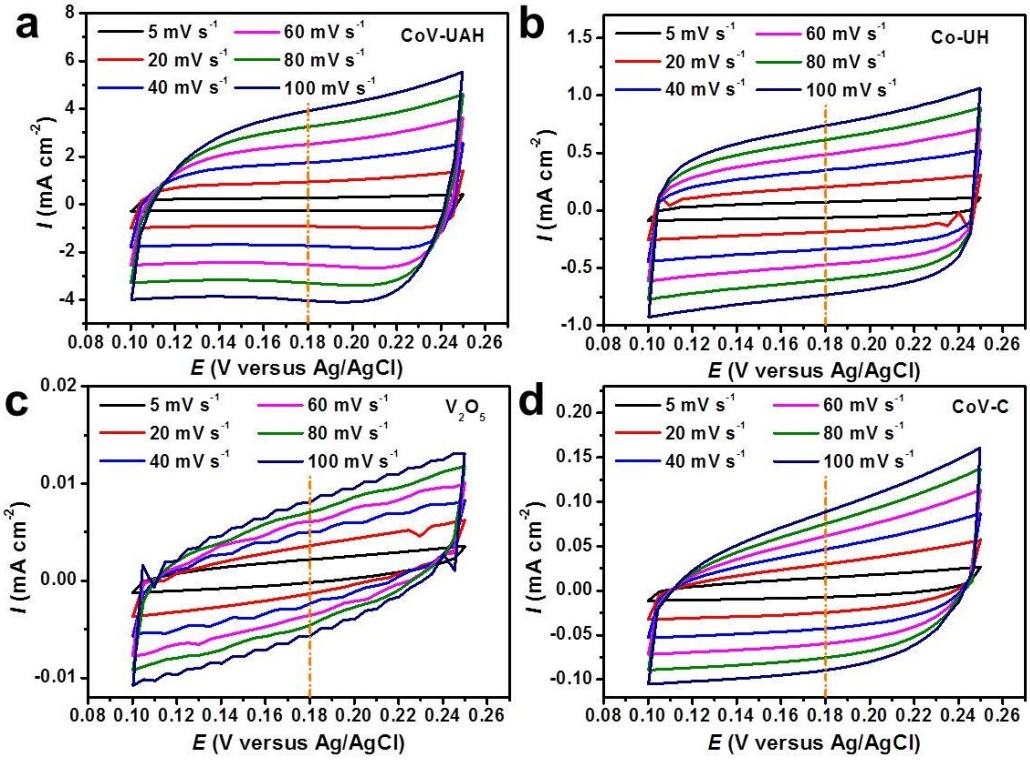

Fig. S18 CVs at different scan rates of in a potential window range from 0.1 to 0.25 V versus Ag/AgCl for the (a) CoV-UAH, (b)Co-UH, (c) V_2O_5 and (d) CoV-C.

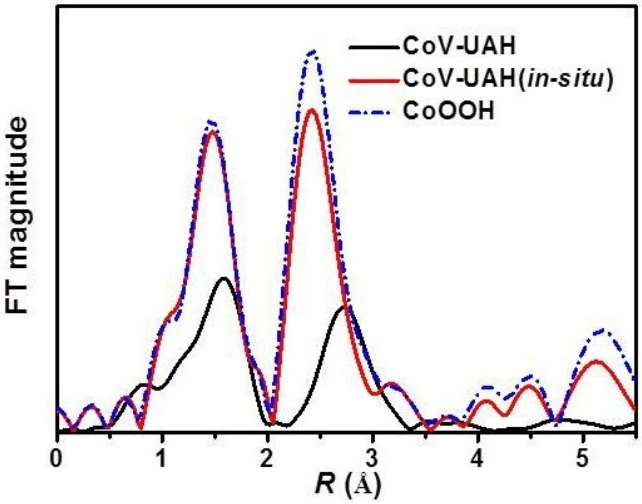

Fig. S19 EXAFS spectra of Co K-edge of CoV-UAH, CoOOH and CoV-UAH at a potential of 1.50 V(CoV-UAH(*in-situ*)). The CoV-UAH(*in-situ*) shows significant decrease in Co-O and Co-Co bond distance which is similar to those of CoOOH. And no splitting peaks which caused by the existence of Co^{2+} species is observed demonstrate the conversion is holistic.

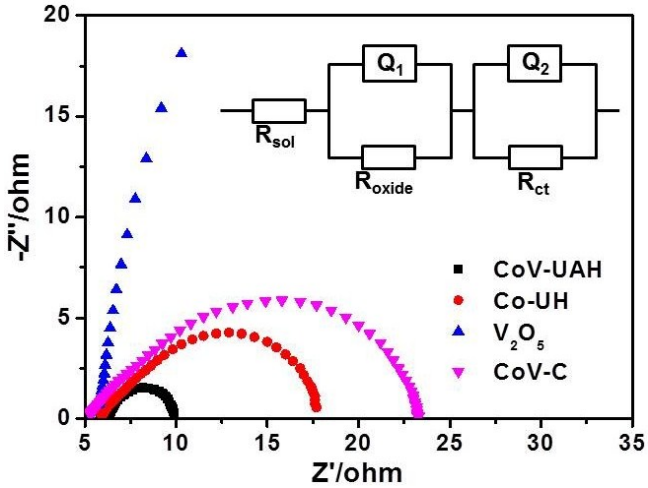

Fig. S20 EIS data for CoV-UAH and counterpart catalysts. The relevant impedance parameter values are shown in Table S3

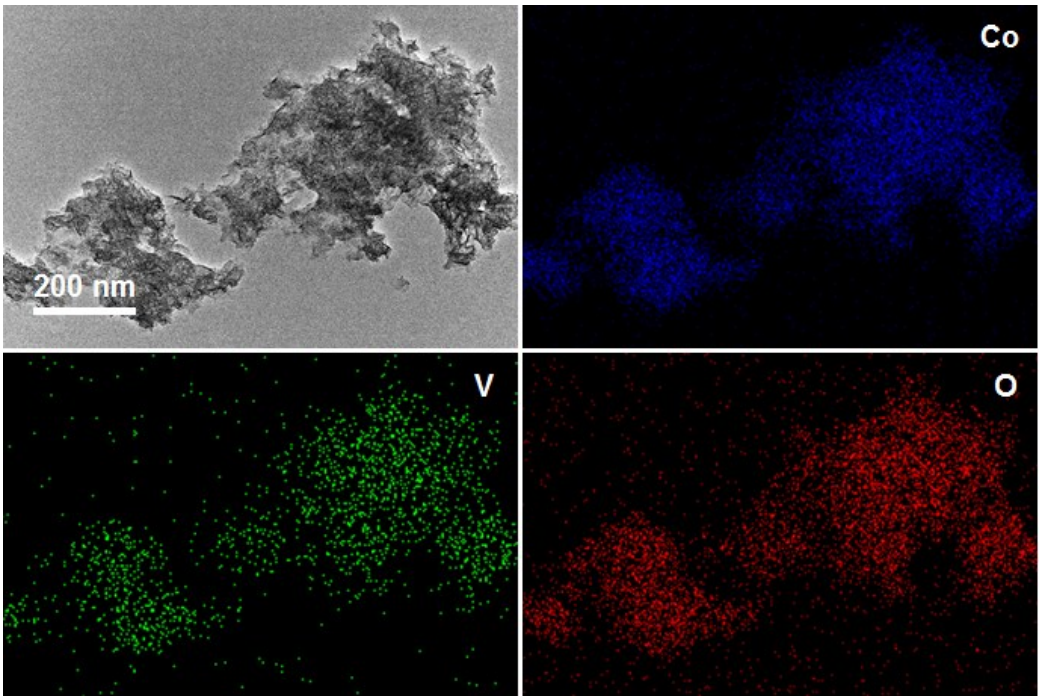

Fig. S21 Morphology and element distribution analysis of CoV-UAH after chronopotentiometry. TEM image shows the stacked nanosheets with wrinkle and crumpled structure. The element mapping demonstrates the dispersion of Co, V and O is homogeneous even though the catalyst went through chronopotentiometry.

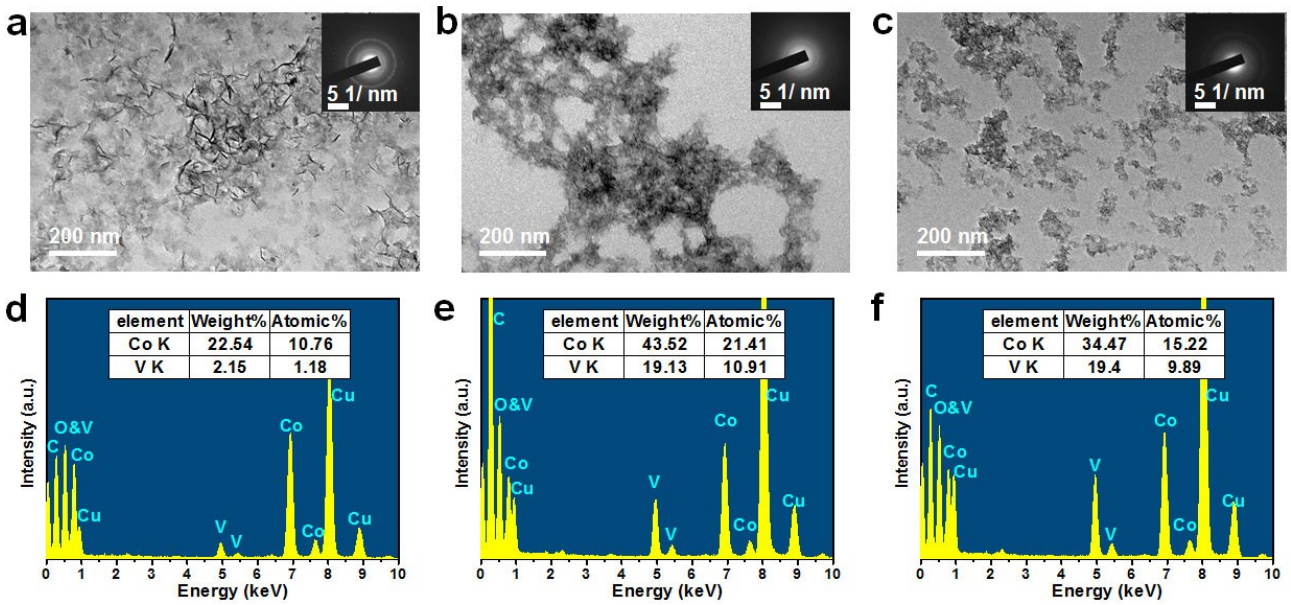

Fig. S22 TEM and relevant EDS analysis of cobalt-vanadium hydr(oxy)oxide at different molecular ratio of Co:V. (a) and (d) Co:V = 10:1 (dosing ratio). (b) and (e) Co:V = 10:5 (dosing ratio). (c) and (f) Co:V = 10:7 (dosing ratio). The TEM images reveal their sheet structure. Distinct diffraction ring is observed in the SAED of Co:V = 10:1 sample, suggesting its polycrystalline structure. The SAED patterns of Co:V = 10:5 and Co:V = 10:7 samples reveal their amorphous structure. The composition ratios obtained from EDS analysis are approximate to the dosing ratios.

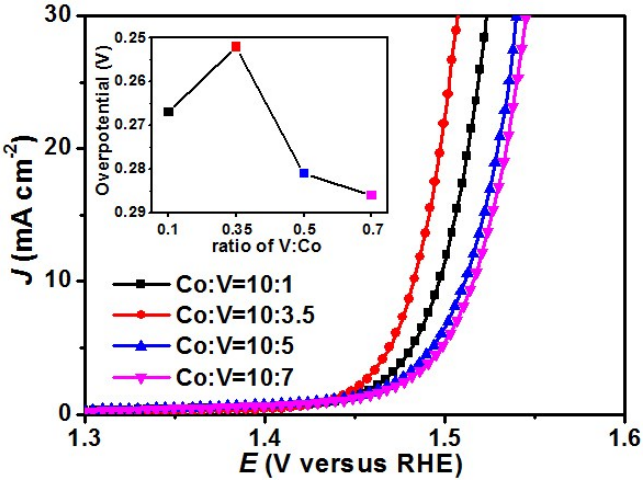

Fig. S23 LSVs of cobalt-vanadium hydr(oxy)oxides in different ratios of Co:V and inset is the relevant overpotential at 10 mA cm^{-2}. Apparently, the optimal proportion of Co:V should be 10:3.5 for its lowest overpotential. When the V percentage increases, the overpotential is instead gradually increased, which suggests excessive V content should reduce the activity.

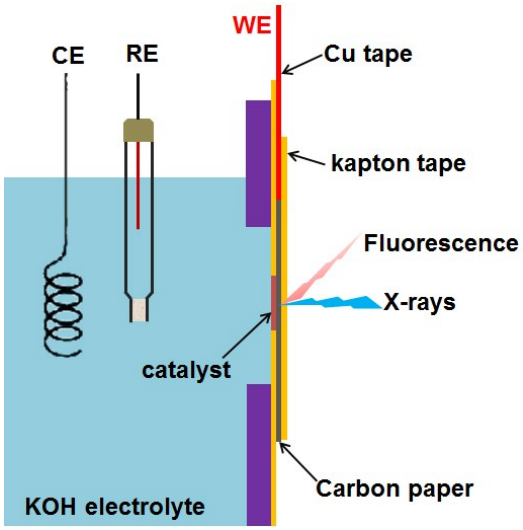

Fig. S24 Schematic diagram of the *in-situ* XAS experiment. As shown, the working electrode was made up with captain tape, carbon paper, and Cu double-faced adhesive tape. We loaded catalyst on carbon paper as working electrode faced into the interior of the electrochemical cell. The electrode was designed to be round shape with a diameter of 8 mm.

Table S1 EXAFS fitting results for the structural parameters around Co and V atoms for the CoV-UAH, $Co(OH)_2$ (R: range from 1.0 to 2.0 Å). CN stands for coordination number; R stands for bonding distance; σ^2 stands for Debye-Waller factor; ΔE stands for edge-energy shift. CoV-UAH shows lower CN (5.4 ± 0.3) and Co-O bonding distance (2.05 ± 0.01) than that of $Co(OH)_2$ (CN (6) and Co-O bonding distance (2.10 ± 0.01)), which indicates lattice distortion and coordination deficiency (*i.e.*, $[CoO_{6-x}]$) occur in the CoV-UAH.

Sample	Scattering pair	CN	R(Å)	σ^2(Å^{-2})	ΔE	R-factor
CoV-UAH	Co-O	5.4 ± 0.3	2.05 ± 0.01	0.009	-5.9	0.0007
$Co(OH)_2$	Co-O	6	2.10 ± 0.01	0.005	-3.4	0.0009
CoV-UAH	V-O	4	1.72 ± 0.01	0.004	-10.3	0.0008

Table S2 Comparison of catalytic parameters of CoV-UAH and counterparts. Here, η(onset) represents onset overpotential versus thermodynamic OER potential (E^0 = 1.23 V versus RHE) defined as the potential required to reach an OER current density of 0.5 mA cm^{-2}. η(10 mA cm^{-2}) stands for overpotential at current density of 10 mA cm^{-2} versus E^0. TOF at η = 0.3 V is representative of the TOF value at an overpotential of 0.3 V. Tafel slopes and linear slopes were obtained from Fig. 3c and Fig. 3d.

sample	η(onset) (mV)	η(10 mA cm^{-2}) (mV)	TOF at η = 0.3 V (s^{-1})	Tafel slope (mV dec^{-1})	linear slope (mF cm^{-2})
CoV-UAH	180	250	0.06882	44	75.87
Co-UH	220	300	0.01276	60	11.87
V_2O_5	320	410	0.00026	44	0.48
CoV-C	270	360	0.00049	63	1.94
IrO_2	240	330	0.01352	48	-

Table S3 Comparison of the AH-Co catalyst with recently-reported state-of-the-art transition-metal-based catalysts.

catalysts	η(10 mA cm^{-2})(V)	Tafel slope (mV dec^{-1})	references
CoV-UAH	**0.25**	**44**	**This work**
monometallic compound catalysts			
oxygen-deficient Co_3O_4 nanorods	0.275	-	Ref. S28
amorphous CoS_x porous nanocubes	0.29	67	Ref. S29
plasma-engraved Co_3O_4 nanosheets	0.3	68	Ref. S30
CoOOH nanosheets	0.3	38	Ref. S5
Co(OH)F	0.313	53	Ref. S31
windmill-shaped spinel Co_3O_4	0.41	-	Ref. S32
single-layer $Ni(OH)_2$	0.32	47	Ref. S33
porous MoO_2 nanosheets	0.3	54	Ref. S34
multimetallic compound catalysts			
Gelled-FeCoW	0.223	37	Ref. S35
NiFe LDH/carbon nanotube	≈0.24	31	Ref. S36
NiCo bimetal-organic framework nanosheets	0.25	42	Ref. S37
ultrathin CoFe LDH nanosheets after Ar plasma etching	0.266	38	Ref. S38
hierarchical Ni-Co-P hollow nanobricks	0.27	76	Ref. S39
oxygen incorporated amorphous cobalt sulfide porous nanocubes	0.29	67	Ref. S40
NiFe nanosheets	0.3	40	Ref. S41
$CoV_{1.5}Fe_{0.5}O_4$ spinel nanocrystals	0.3	38	Ref. S42
$CuCo_2S_4$ nanosheets	0.31	86	Ref. S43
Ni-Co bimetal phosphide nanocages	0.3	80	Ref. S44
$Ni_{0.75}V_{0.25}$-LDH	≈0.32	50	Ref. S45
$Zn_xCo_{3-x}O_4$	0.32	51	Ref. S46
CoMn LDH	0.324	43	Ref. S47
$Ni_{0.75}Co_{0.25}O_x$	≈0.345	33±1	Ref. S48
$Co_3V_2O_8$ with one-dimensional morphology on nanotubes and nanorods	0.350	46	Ref. S49
$Co_3V_2O_8$ nanoparticles	0.359	65	Ref. S2
$Ba_{0.5}Sr_{0.5}Co_{0.8}Fe_{0.2}$	≈0.362	48	Ref. S26

Fe–mesoporous Co_3O_4	0.38	60	Ref. S50
composite catalysts			
Co_3O_4/N-doped reduced graphene oxide	0.31	67	Ref. S51
CoO_x/B,N-decorated graphene	0.295	57	Ref. S52
Fe-CoOOH/graphene	0.33	37	Ref. S53

The data were obtained in 1 M KOH without specific mention. LDH stands for layered double hydroxide.

Table S4 Impedance parameter values derived from the fitting to the equivalent circuit for the impedance spectra recorded in 1.0 M KOH solution.[S54,55] Here, the solution resistance, oxide film resistance and charge-transfer resistance are denoted as R_{sol}, R_{oxide}, and R_{ct}. Capacitive elements are replaced by constant phase elements (CPE), denoted by Q and employed for fitting the experimental data. Q_1 denotes CPE of catalyst layer and Q_2 represents the double layer capacitance.

sample	R_{sol}	Q_1	n	R_{oxide}	Q_2	n	R_{ct}
CoV-UAH	5.548	0.01516	0.8	0.9569	0.01676	0.9573	3.381
Co-UH	5.859	0.003875	0.6512	0.3347	0.001931	0.9146	8.683
V_2O_5	5.627	6.22E-05	0.841	125.9	1.84E-05	0.8	47.77
CoV-C	5.144	0.000641	0.8683	11.91	0.002054	0.587	63.8

3. References

S1 G. Li, K. Chao, H. Peng, A. Kezheng Chen and Z. Zhang, *Inorg. Chem.*, 2007, **46**, 5787.
S2 M. Xing, L. B. Kong, M. C. Liu, L. Y. Liu, L. Kang and Y. C. Luo, *J. Mater. Chem. A*, 2014, **2**, 18435.
S3 Z. P. Liu, R. Z. Ma, M. Osada, K. Takada and T. Sasaki, *J. Am. Chem. Soc.*, 2005, **127**, 13869.
S4 F. Bardé, M. R. Palacin, B. Beaudoin, A. Delahaye-Vidal and J. M. Tarascon, *Chem. Mater.*, 2004, **16**, 299.
S5 J. H. Huang, J. T. Chen, T. Yao, J. F. He, S. Jiang, Z. H. Sun, Q. H. Liu, W. R. Cheng, F. C. Hu, Y. Jiang, Z. Y. Pan and S. Q. Wei, *Angew. Chem. Int. Ed.*, 2015, **54**, 8722.
S6 B. Ravel and M. Newvile, *J. Synchrotron Radiat.*, 2005, **12**, 537.
S7 D. Koningsberger and R. Prins, *John Wiley & Sons, New York*, 1988, **92**, 257.
S8 B. Ravel and M. Newville, *Phys. Scr.*, 2005, **T115**, 1007.
S9 A. L. Ankudinov, B. Ravel, J. J. Rehr and S. D. Conradson, *Phys. Rev. B*, 1998, **58**, 7565.
S10 L. Cai, J. He, Q. Liu, T. Yao, L. Chen, W. Yan, F. Hu, Y. Jiang, Y. Zhao, T. Hu, Z. Sun and S. Wei, *J. Am. Chem. Soc.*, 2015, **137**, 2622.
S11 M. Risch, F. Ringleb, M. Kohlhoff, P. Bogdanoff, P. Chernev, I. Zaharieva and H. Dau, *Energy Environ. Sci.*, 2015, **8**, 661.
S12 M. W. Kanan, J. Yano, Y. Surendranath, M. Dincă, V. K. Yachandra and D. G. Nocera, *J. Am. Chem. Soc.*, 2010, **132**, 13692.
S13 M. W. Kanan and D. G. Nocera, *Science*, 2008, **39**, 1072.
S14 G. Kresse and J. Hafner, *Phys. Rev. B*, 1993, **47**, 558.
S15 G. Kresse and J. Hafner, *Phys. Rev. B: Condens. Matter*, 1994, **49**, 14251.
S16 G. Kresse and J. Furthmüller, *Phys. Rev. B: Condens. Matter*, 1996, **54**, 11169.
S17 G. Kresse and J. Furthmüller, *Comp. Mater. Sci.*, 1996, **6**, 15.
S18 J. P. Perdew, K. Burke and M. Ernzerhof, *Phys. Rev. Lett.*, 1996, **77**, 3865.
S19 B. PE, *Phys. Rev. B: Condens. Matter*, 1994, **50**, 17953.
S20 M. Bajdich, M. Garcíamota, A. Vojvodic, J. K. Nørskov and A. T. Bell, *J. Am. Chem. Soc.*, 2013, **135**, 13521.
S21 S. L. Dudarev, G. A. Botton, S. Y. Savrasov, C. J. Humphreys and A. P. Sutton, *Phys. Rev. B*, 1998, **57**, 1505.
S22 N. J. Mosey, P. Liao and E. A. Carter, *Phys. Rev. B: Condens. Matter*, 2008, **129**, 014103.
S23 A. E. Bocquet, T. Mizokawa, K. Morikawa, A. Fujimori, S. R. Barman, K. Maiti, D. D. Sarma, Y. Tokura and M. Onoda, *Phys. Rev. B: Condens. Matter*, 1992, **46**, 3771.
S24 L. Wang, T. Maxisch and G. Ceder, *Phys. Rev. B*, 2006, **73**, 195107.
S25 I. C. Man, H. Y. Su, F. Calle‐Vallejo, H. A. Hansen, J. I. Martinez, N. G. Inoglu, J. Kitchin, T. F. Jaramillo, J. K. Nørskov and J. Rossmeisl, *Chemcatchem*, 2011, **3**, 1085.
S26 J. Suntivich, K. J. May, H. A. Gasteiger, J. B. Goodenough and Y. Shao-Horn, *Science*, 2011, **334**, 1383.
S27 M. Ghiyasiyan-Arani, M. Masjedi-Arani and M. Salavati-Niasari, *J. Mol. Catal. A Chem.*, 2016, **425**, 31.
S28 G. Cheng, T. Kou, J. Zhang, C. Si, H. Gao and Z. Zhang, *Nano Energy*, 2017, **38**, 155.
S29 P. Cai, J. Huang, J. Chen and Z. Wen, *Angew. Chem. Int. Ed.*, 2017, **56**, 4858.
S30 L. Xu, Q. Q. Jiang, Z. H. Xiao, X. Y. Li, J. Huo, S. Y. Wang and L. M. Dai, *Angew. Chem. Int. Ed.*, 2016, **128**, 5363.
S31 S. Wan, J. Qi, W. Zhang, W. Wang, S. Zhang, K. Liu, H. Zheng, J. Sun, S. Wang and R. Cao, *Adv. Mater.*, 2017, **29**, 1700286.
S32 L. Zhang, W. H. He, X. Xiang, Y. Li and F. Li, *RSC Adv.*, 2014, **4**, 43357.
S33 L. Wang, C. Lin, D. K. Huang, F. X. Zhang, M. K. Wang and J. Jin, *ACS Appl. Mater. Interfaces*, 2014, **6**, 10172.
S34 Y. S. Jin, H. T. Wang, J. J. Li, X. Yue, Y. J. Han, P. K. Shen and Y. Cui, *Adv. Mater.*, 2016, **28**, 3785.
S35 B. Zhang, X. L. Zheng, O. Voznyy, R. Comin, M. Bajdich, M. Garcia-Melchor, L. L. Han, J. X. Xu, M. Liu, L. R. Zheng, F. P. Garcia de Arquer, C. T. Dinh, F. J. Fan, M. J. Yuan, E. Yassitepe, N. Chen, T. Regier, P. F. Liu, Y. H. Li, P. De Luna, A. Janmohamed, H. L. Xin, H. G. Yang, A. Vojvodic and E. H. Sargent, *Science*, 2016, **352**, 333.
S36 M. Gong, Y. G. Li, H. L. Wang, Y. Y. Liang, J. Z. Wu, J. G. Zhou, J. Wang, T. Regier, F. Wei and H. J. Dai, *J. Am. Chem. Soc.*, 2013, **135**, 8452.
S37 S. L. Zhao, Y. Wang, J. C. Dong, C.-T. He, H. J. Yin, P. F. An, K. Zhao, X. F. Zhang, C. Gao, L. J. Zhang, J. W. Lv, J. X. Wang, J. Q. Zhang, A. M. Khattak, N. A. Khan, Z. X. Wei, J. Zhang, S. Q. Liu, H. J. Zhao and Z. Y. Tang, *Nat. Energy*, 2016, **1**, 16184
S38 Y. Wang, Y. Zhang, Z. Liu, C. Xie, S. Feng, D. Liu, P. M. Shao and P. S. Wang, *Angew. Chem. Int. Ed.*, 2017, **129**, 1.
S39 E. Hu, Y. Feng, J. Nai, D. Zhao, Y. Hu and X. W. Lou, *Energy Environ. Sci.*, 2018, DOI: 10.1039/C8EE00076J.
S40 P. Cai, J. Huang, J. Chen and Z. Wen, *Angew. Chem. Int. Ed.*, 2017, **56**, 1.
S41 F. Song and X. L. Hu, *Nat. Commun.*, 2014, **5**, 4477.
S42 K. Chakrapani, G. Bendt, H. Hajiyani, T. Lunkenbein, M. Greiner, L. Masliuk, S. Salamon, J. Landers, R. Schloegl, H. Wende, R. Pentcheva, S. Schulz and M. Behrens, *ACS Catal.*, 2018, **8**, 1259.
S43 M. Chauhan, K. P. Reddy, C. S. Gopinath and S. Deka, *ACS Catal.*, 2017, **7**, 5871.
S44 B. Qiu, L. Cai, Y. Wang, Z. Lin, Y. Zuo, M. Wang and a. Y. Chai, *Adv. Funct. Mater.*, 2018, **1706008**.
S45 K. Fan, H. Chen, Y. Ji, H. Huang, P. M. Claesson, Q. Daniel, B. Philippe, H. Rensmo, F. Li, Y. Luo and L. Sun, *Nat. Commun.*, 2016, **7**, 11981.
S46 X. J. Liu, Z. Chang, L. Luo, T. H. Xu, X. D. Lei, J. F. Liu and X. M. Sun, *Chem. Mater.*, 2014, **26**, 1889.
S47 F. Song and X. L. Hu, *J. Am. Chem. Soc.*, 2014, **136**, 16481.
S48 L. Trotochaud, J. K. Ranney, K. N. Williams and S. W. Boettcher, *J. Am. Chem. Soc.*, 2012, **134**, 17253.
S49 S. Hyun, V. Ahilan, H. Kim and S. Shanmugam, *Electrochem. Commun.*, 2015, **63**, 44.
S50 C. L. Xiao, X. Y. Lu and C. Zhao, *Chem. Commun.*, 2014, **50**, 10122.
S51 Y. Y. Liang, Y. G. Li, H. L. Wang, J. G. Zhou, J. Wang, T. Regier and H. J. Dai, *Nat. Mater.*, 2011, **10**, 780.
S52 Y. Tong, P. Chen, T. Zhou, K. Xu, W. Chu, C. Wu and Y. Xie, *Angew. Chem. Int. Ed.*, 2017, **56**, 1.
S53 X. Han, C. Yu, S. Zhou, C. Zhao, H. Huang, J. Yang, Z. Liu, J. Zhao and J. Qiu, *Adv. Energy Mater.*, 2017, **7**, 1602148.
S54 F. Hu, S. Zhu, S. Chen, Y. Li, L. Ma, T. Wu, Y. Zhang, C. Wang, C. Liu, X. Yang, L. Song, X. Yang and Y. Xiong, *Adv. Mater.*, 2017, **29**, 1606570.
S55 A. Irshad and N. Munichandraiah, *ACS Appl. Mater. Interfaces*, 2015, **7**, 15765.